An In Situ Study of Turbulence near Stellar Bow Shocks

Stella Koch Ocker[1] , James M. Cordes[1] , Shami Chatterjee[1] , and Timothy Dolch[2,3]

[1] Department of Astronomy and Cornell Center for Astrophysics and Planetary Science, Cornell University, Ithaca, NY 14853, USA; sko36@cornell.edu
[2] Department of Physics, Hillsdale College, 33 East College Street, Hillsdale, MI 49242, USA
[3] Eureka Scientific, Inc., 2452 Delmer Street, Suite 100, Oakland, CA 94602-3017, USA

Abstract

Stellar bow shocks are observed in a variety of interstellar environments and shaped by the conditions of gas in the interstellar medium (ISM). In situ measurements of turbulent density fluctuations near stellar bow shocks are only achievable with a few observational probes, including Hα-emitting bow shocks and the Voyager Interstellar Mission (VIM). In this paper, we examine density variations around the Guitar Nebula, an Hα bow shock associated with PSR B2224+65, in tandem with density variations probed by VIM near the boundary of the solar wind and ISM. High-resolution Hubble Space Telescope observations of the Guitar Nebula taken between 1994 and 2006 trace density variations over scales from hundreds to thousands of au, while VIM density measurements made with the Voyager 1 Plasma Wave System constrain variations from thousands of meters to tens of au. The power spectrum of density fluctuations constrains the amplitude of the turbulence wavenumber spectrum near the Guitar Nebula to $\log_{10} C_n^2 = -0.8 \pm 0.2$ m$^{-20/3}$ and for the very local ISM probed by Voyager to $\log_{10} C_n^2 = -1.57 \pm 0.02$ m$^{-20/3}$. Spectral amplitudes obtained from multiepoch observations of four other Hα bow shocks also show significant enhancements from values that are considered typical for the diffuse, warm ionized medium, suggesting that density fluctuations near these bow shocks may be amplified by shock interactions with the surrounding medium or selection effects that favor Hα emission from bow shocks embedded in denser media.

Unified Astronomy Thesaurus concepts: Stellar bow shocks (1586); Interstellar medium (847); Neutron stars (1108); Pulsars (1306); Heliosphere (711); Astrosphere interstellar medium interactions (106)

1. Introduction

Bow shocks form around stars moving at supersonic and super-Alfvénic speeds through the interstellar medium (ISM), and their morphologies are determined by the conditions for ram pressure balance between their stellar winds and the surrounding interstellar gas. Bow shocks are observed around stars at a range of life stages, including runaway OB stars (Peri et al. 2012, 2015) and supergiants (Decin et al. 2012), and their signatures are observed over wavelengths spanning radio to X-rays. Neutron stars, in particular, are believed to generally produce bow shocks, as they are born at speeds ranging from hundreds to thousands of kilometers per second and typically move faster than the speed of sound once they have exited their supernova remnants and entered the ambient ISM. Currently, one of the only direct methods for detecting neutron star bow shocks is by observing the Hα emission that is produced by collisional excitation of interstellar gas at the bow shock, but this method requires that the gas be partially neutral, and Hα bow shocks have only been observed from about nine neutron stars thus far (Brownsberger & Romani 2014). Observations of nonthermal radio and X-ray emission from ram pressure–confined pulsar wind nebulae have provided indirect evidence for the presence of bow shocks around an additional handful of neutron stars (Kargaltsev et al. 2017), but unlike Hα-emitting bow shocks, these observations do not yield direct measurements of the bow shock standoff radius. Far-ultraviolet emission from pulsar bow shocks may also yield estimates of the standoff radius but has only been detected from two pulsars thus far (Rangelov et al. 2016, 2017). Since the standoff radius is directly related to the interstellar gas density, Hα measurements of the bow shock standoff radius over time are thus one of the only

direct probes of turbulent density fluctuations in the partially ionized ISM.

This method is perhaps best exemplified by the Guitar Nebula (GN), the unusually shaped bow shock formed around the radio pulsar B2224+65. The GN was initially detected with the 5 m Palomar telescope in Hα emission extending over about an arcminute on the sky (Cordes et al. 1993), and follow-up observations of the bow shock nose with the Hubble Space Telescope (HST) in 1994 and 2001 were able to resolve changes in the standoff radius and interstellar density over the 7 yr timescale (Chatterjee & Cordes 2002, 2004). Observations with the Discovery Channel Telescope in 2014 demonstrated continued large-scale evolution of the entire nebula, consistent with an expansion rate of about 200 km s^{-1} (Dolch et al. 2016, T. Dolch et al. 2021, in preparation). Magnetohydrodynamic modeling has confirmed that the bow shock's large-scale, quasi-oscillatory morphology can be predominantly ascribed to density variations in the surrounding medium (Yoon & Heinz 2017; Toropina et al. 2019; Barkov et al. 2020). However, the detection of multiple glitches in the pulsar's spin period (Janssen & Stappers 2006; Yuan et al. 2010) also raises the question of whether changes in the pulsar's spin-down luminosity can modify the observed bow shock and how, if at all, the pulsar wind modifies density fluctuations in the surrounding ISM (Chatterjee & Cordes 2002; Dolch et al. 2016).

Pulsar bow shocks are not the only in situ probe of turbulent density fluctuations in the ISM. The Voyager Interstellar Mission (VIM) spacecraft Voyager 1 and Voyager 2 (V1/V2) both directly sample electron density fluctuations in the very local ISM (VLISM), a region of space beyond the heliopause that is the boundary at which the solar wind and interstellar plasma reach pressure balance. The structure of the outer

heliosphere and VLISM can be broadly divided into three main regions: the termination shock, where the solar wind slows to subsonic speeds; the heliopause (i.e., the contact discontinuity), which is taken to be the boundary of the heliosphere; and a bow shock that sweeps up and decelerates the interstellar wind (e.g., Opher 2016). The exact nature of the heliosphere's bow shock, if it exists, is unclear. Measurements of the Sun's velocity with respect to the VLISM made by the Interstellar Boundary Explorer initially suggested that the velocity is below the fast magnetosonic speed (McComas et al. 2012), implying that under certain conditions (such as a strong magnetic field of $\sim 4\,\mu G$), no bow shock would be present (Zank et al. 2013). However, more recent measurements have revised the interstellar flow velocity to about $26\,km\,s^{-1}$ (McComas et al. 2015; Swaczyna et al. 2018), above the nominal fast magnetosonic speed. Moreover, different configurations of the interstellar flow velocity, magnetic field, and densities of ionized and neutral hydrogen can give rise to heliospheric bow shocks or bow waves exhibiting a wide range of properties (Zank et al. 2013; Zieger et al. 2013). Recent study of magnetic turbulence with VIM suggests that VLISM turbulence follows a Kolmogorov spectrum with an outer scale of about 0.01 pc, which is broadly consistent with theoretical predictions for the distance to the bow wave/shock (Burlaga et al. 2018; Lee & Lee 2020).

Regardless of the heliospheric bow shock's unresolved nature, direct sampling of the ISM with both VIM and the GN offers a unique opportunity to study turbulent plasma near the boundaries between stellar winds and their interstellar environments across a wide range of physical conditions. While Voyager can probe density fluctuations on scales as small as a kilometer, Hα images of the GN reveal density fluctuations across the bow shock's entire historical trajectory up to $\sim$0.1 pc. The heliosphere is moving at approximately $26\,km\,s^{-1}$ relative to the local interstellar plasma flow, whereas the GN is generated by a pulsar moving at $770\,km\,s^{-1}$ (Deller et al. 2019). The local interstellar environments in both cases are also potentially quite different. The heliosphere lies near the edge of a partially ionized cloud within the Local Bubble (Linsky et al. 2019). The GN, by contrast, is 831 pc away and lies about 6° above the Galactic plane, in an extended region of warm, partially ionized gas that exhibits complicated filamentary structure (Chatterjee & Cordes 2002).

In this paper, we examine direct measurements of electron density fluctuations near stellar bow shocks using Hα images of the GN and data taken by the V1 Plasma Wave System (PWS) instrument. In Section 2, we outline how the wavenumber spectrum of turbulent density fluctuations can be constrained by both in situ and integrated electron density measurements. A description of the HST observations of the GN is provided in Section 3; our analysis of the Guitar includes a third HST epoch from 2006. Observed variations in the bow shock morphology are analyzed in Section 4, and a new parallax distance for B2224+65 obtained through high-precision very long baseline interferometry (Deller et al. 2019) allows us to place more precise constraints on the bow shock standoff radius. In Section 4.2, we consider the impact of pulsar glitches on the bow shock and find that even the largest glitch observed from B2224+65 would have had negligible impact on the observed bow shock structure. In Section 5, we discuss high-resolution density measurements obtained by V1 PWS. Finally, in Section 6, constraints on the density wavenumber spectrum

from the GN and V1 are discussed in the context of density fluctuations observed along pulsar lines of sight (LOSs) throughout the local ISM, including four other neutron star bow shocks. Conclusions and remarks on future work are provided in Section 7.

2. Density Wavenumber Spectrum

The wavenumber spectrum of electron density (n_e) fluctuations is modeled as a power law of the form

$$P_{\delta n_e} = C_n^2 q^{-\beta}, \quad q_o \leqslant q \leqslant q_i, \tag{1}$$

where $\beta = 11/3$ for Kolmogorov turbulence, C_n^2 is the spectral amplitude, and q is the wavenumber, which is related to the length scale L by $q = 2\pi/L$. The spectrum extends from the outer scale $q_o = 2\pi/l_o$ to the inner scale $q_i = 2\pi/l_i$.

2.1. In Situ Density Measurements

In situ density measurements at two epochs ($n_{e,1}$, $n_{e,2}$) correspond to a spatial offset $\delta x = v(t_2 - t_1)$, where v is the velocity of the spacecraft or pulsar. A pairwise estimate of the density structure function is then

$$\widehat{D}_{n_e} = \langle [n_e(\boldsymbol{x}) - n_e(\boldsymbol{x} + \delta \boldsymbol{x})]^2 \rangle \approx (n_{e1} - n_{e2})^2. \tag{2}$$

The model density structure function D_{n_e} is related to the autocorrelation function (ACF) R_{n_e} as $D_{n_e}(\delta \boldsymbol{x}) = 2[R_{n_e}(0) - R_{n_e}(\delta \boldsymbol{x})]$, where the ACF is given by

$$R_{n_e}(\delta \boldsymbol{x}) = \int d\boldsymbol{q} \, e^{i(\boldsymbol{q} \cdot \delta \boldsymbol{x})} P_{\delta n_e}(\boldsymbol{q}). \tag{3}$$

Integrating over the 3D wavenumber spectrum thus yields an analytic relationship between the density structure function and the spectral amplitude:

$$D_{n_e}(\delta \boldsymbol{x}) = 2 \int d\boldsymbol{q} (1 - e^{i(\boldsymbol{q} \cdot \delta \boldsymbol{x})}) P_{\delta n_e}(\boldsymbol{q}). \tag{4}$$

For an isotropic wavenumber spectrum and $q_o \gg 2\pi/\delta x \gg q_i$, $D_{n_e} = K_{n_e}(\beta) C_n^2 \ (\delta x)^{\beta-3}$, where $K_{n_e}(\beta) = 4\pi \Gamma(\beta/2 - 1) \Gamma(4 - \beta) \cos(\pi(\beta - 3)/2)/(\beta - 3)\Gamma(\beta/2) \approx 20$ for $\beta = 11/3$ and $K_{n_e} = 2\pi^2$ for $\beta = 4$. Individual point estimates of the spectral amplitude $\widehat{C}_n^2$ and wavenumber $\widehat{q}$ can then be obtained as

$$\widehat{C}_n^2 \approx \frac{\widehat{D}_{n_e}(\delta \boldsymbol{x})}{K_{n_e}(\beta)(\delta x)^{\beta-3}}, \quad \widehat{q} \approx 2\pi/\delta x. \tag{5}$$

A distribution of point estimates $\widehat{C}_n^2$ can then be fit for a characteristic value, which we denote as C_n^2. In the analysis that follows, we adopt the Kolmogorov spectral index $\beta = 11/3$ as a fiducial value for directly estimating $\widehat{C}_n^2$ from density measurements based on substantial evidence that turbulence in both the ambient ionized ISM and the VLISM is consistent with this assumption (Armstrong et al. 1995; Chepurnov & Lazarian 2010; Burlaga et al. 2018; Lee & Lee 2020).

2.2. Integrated Density Measurements

Pulsar timing observations yield measurements of the integrated electron density or dispersion measure DM$= \int_0^D n_e \, dl$ along the LOS to a pulsar at a distance D. Prolonged timing campaigns by pulsar timing arrays sample the DMs

of ∼80 pulsars about once a month over months- to decades-long time spans (e.g., Alam et al. 2021). The observed DM variations over time DM(*t*) can be used to trace stochastic density fluctuations along a pulsar LOS and hence constrain the wavenumber spectrum, but doing so requires correcting for deterministic DM variations that arise from the pulsar LOS crossing discrete structures in the ISM (Lam et al. 2016; Jones et al. 2017). In the absence of these deterministic contributions to DM(*t*), the DM structure function $D_{\mathrm{DM}}(\tau) = \langle [\mathrm{DM}(t+\tau) - \mathrm{DM}(t)]^2 \rangle$ is directly related to the rms of the DM variations, which can be related to the amplitude of the density wavenumber spectrum as

$$\widehat{C}_{\mathrm{n}}^2 = \frac{1}{K_{\mathrm{DM}}} \left[\frac{D_{\mathrm{DM}}(\tau)}{D(v_{\mathrm{eff},\perp}\tau)^{\beta-2}} \right], \quad \widehat{q} \approx 2\pi/(v_{\mathrm{eff},\perp}\tau), \qquad (6)$$

where τ is the time lag between two point estimates of DM, $K_{\mathrm{DM}} \approx 88.3$ for $\beta = 11/3$, D is the distance to the pulsar, and $v_{\mathrm{eff},\perp}$ is the pulsar's effective transverse velocity, which is related to the transverse velocities of the pulsar, observer, and interstellar phase screen (Lam et al. 2016). For a Kolmogorov process, the DM structure function has the form $D_{\mathrm{DM}}(\tau) \sim \tau^{5/3}$.

3. Observations of the GN

High-resolution observations of the GN were obtained with HST in 1994 December and 2001 December using the Wide Field Planetary Camera 2 (WFPC2). The details of these observations have already been discussed in Chatterjee & Cordes (2002, 2004). A third HST epoch was obtained in 2006 using the Advanced Camera for Surveys (ACS; Gautam et al. 2013). Figure 1 shows the Hα images from all three epochs, which were aligned using the three brightest reference stars in each frame, in addition to a large-scale image of the Guitar taken at Palomar Observatory in 1995 (Chatterjee & Cordes 2002). Between 1994 and 2001, the tip of the bow shock moved 1″32, equivalent to 1097 au, and between 2001 and 2006, the bow shock moved 0″86, equivalent to 715 au. The motion of the bow shock nose is consistent with the pulsar proper motion (see Table 1).

The shape of the bow shock nose can be directly inferred from the Hα images and used to constrain the bow shock standoff radius. In the thin-shell limit, the radial shape of the bow shock can be expressed as (Wilkin 1996)

$$R(\theta) = R_0 \csc\theta \sqrt{3(1 - \theta\cot\theta)}, \qquad (7)$$

where R_0 is the standoff radius and θ represents the angle between the pulsar's velocity and a point $R(\theta)$ along the bow shock. The standoff radius is dictated by the pressure balance between the ambient ISM and the neutron star wind and directly related to the interstellar density ρ_A, the pulsar wind velocity v_w and mass-loss rate $\dot{m}_w$, and the pulsar velocity v_p (Wilkin 1996):

$$R_0 = \left(\frac{\dot{m}_w v_w}{4\pi\rho_A v_p^2} \right)^{1/2}. \qquad (8)$$

Equation (8) assumes an isotropic stellar wind, which is not generally true of a relativistic neutron star wind. When the pulsar rotation vector is skewed relative to the pulsar proper motion and magnetic field, the pulsar wind will be quasi-isotropic, and its exact behavior will depend on both the orientations of these vectors and the opening angle of the wind. For B2224+65, the light-cylinder radius is significantly smaller than the bow shock standoff radius, suggesting that an isotropic wind is an adequate assumption without additional evidence for anisotropy (for a detailed discussion, see Chatterjee & Cordes 2002). Assuming that the spin-down energy loss is entirely carried by the relativistic wind, $\dot{m}_w v_w = \dot{E}/c$. The standoff radius can be conveniently reformulated as an angle given by

$$\theta_0 = 56.3 \ \mathrm{mas} \left(\frac{\sin^2 i}{n_A^{1/2}} \right) \left(\frac{\dot{E}_{33}^{1/2}}{\mu_{100} D_{\mathrm{kpc}}^2} \right), \qquad (9)$$

where i is the inclination angle, $n_A = \rho_A/m_{\mathrm{H}}$ is the total number density of the interstellar hydrogen and helium mixture in atomic mass units per cubic centimeter, $\dot{E}$ is the spin-down luminosity in erg per second, D is the distance to the pulsar in kiloparsecs, and μ_{100} is the pulsar proper motion in 100 mas yr^{-1} (Chatterjee & Cordes 2002). The spin-down luminosity is $\dot{E} = 4\pi^2 I\dot{P}/P^3$, where $I \approx 10^{45}$ g cm^2. The period derivative $\dot{P}$ can be corrected for the Schklovskii effect using

$$\dot{P} = \dot{P}_{\mathrm{obs}} - 2.43 \times 10^{-21} P\mu_{\mathrm{masy}}^2 D_{\mathrm{kpc}}, \qquad (10)$$

where μ_{masy} is the proper motion in milliarcseconds per year (Shklovskii 1970; Brownsberger & Romani 2014). This correction is negligible for B2224+65. The atomic number density n_A is converted to an electron density n_e assuming a cosmic abundance $\gamma_{\mathrm{H}} = 1.37$, where $n_A = n_{\mathrm{H}}\gamma_{\mathrm{H}}$ and $n_{\mathrm{H}} \approx n_e$. The standoff angle that is inferred from the outer edge of the Hα emission corresponds to a forward shock that lies slightly upstream of the contact discontinuity at an angular distance $\theta_a \approx 1.3\theta_0$ (Aldcroft et al. 1992; Bucciantini 2002). The period, period derivative, and spin-down luminosity for B2224+65 are shown in Table 1.

4. Turbulence around the Guitar

4.1. Variations in the Standoff Radius

Variations in the bow shock standoff radius over time for the GN are predominantly related to density fluctuations in the surrounding gas over the length scales traversed by the pulsar between observations. Changes in the pulsar wind velocity and mass-loss rate may also impact variations in the standoff radius but are likely insignificant on the scales probed by the Hα observations (see Section 4.2). The outline of the bow shock nose was extracted from each Hα image by tracing local maxima in Hα intensity along the edge of the shock and is shown in Figure 2. Between 1994 and 2006, the bow shock nose moved 2″18, a total distance of 1812 au. While the overall morphology of the bow shock indicates a highly inhomogeneous interstellar density, the nose of the bow shock is adequately described by the thin-shell approximation given in Equation (7) to within about 2″ of the nose. The projected angular apex distance θ_a was fit to the bow shock outline extracted from each HST epoch (see Figure 2) using least-squares minimization of the χ^2 statistic $\sum_{i=1}^{N}(M_i - D_i)^2/D_i^2$, where M_i is the Wilkin (1996) model prediction for the location of a given point along the bow shock given by Equation (7), and D_i is the corresponding location of a point along the observed shock. Given the extremely large transverse velocity
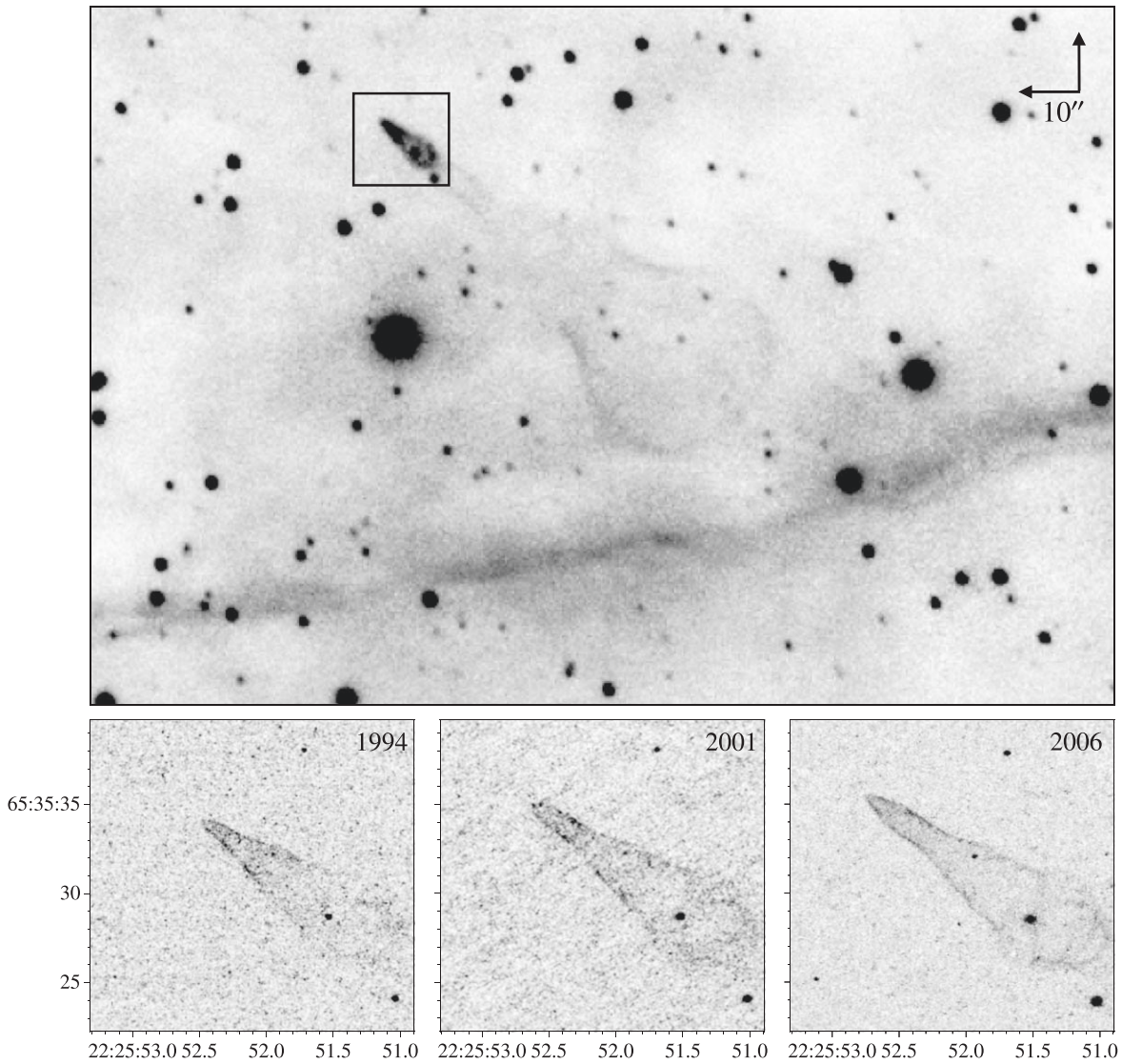
Figure 1. Top: Hα image of the GN observed with the 5 m Hale Telescope at Palomar Observatory in 1995, previously discussed in Chatterjee & Cordes (2002, 2004). The black inset indicates the region shown in the bottom panels. The compass indicates north and east. Bottom: Hα images of the head of the GN observed by HST in 1994, 2001, and 2006. The 1994 and 2001 images were taken by WFPC2, and the 2006 image was taken by ACS. The 1994 and 2001 epochs were previously discussed in Chatterjee & Cordes (2002, 2004).

of this pulsar, we do not consider the radial component of the pulsar velocity when fitting the apex shape. The apex distance is $0''.077(4)$ in 1994, $0''.11(1)$ in 2001, and $0''.094(6)$ in 2006. Given negligible epoch-to-epoch changes in inclination angle, spin-down luminosity (see Section 4.2), proper motion, and distance, the ratio of the apparent standoff angles between epochs gives the change in number density $\theta_{0,1}/\theta_{0,2} = \sqrt{n_{A,2}/n_{A,1}}$. We find $n_{A,2001}/n_{A,1994} = 0.5(1)$, $n_{A,2006}/n_{A,2001} = 1.4(3)$, and $n_{A,2006}/n_{A,1994} = 0.7(1)$. The first value is broadly consistent with the decrease in density found by Chatterjee & Cordes (2004), and the additional density increase between 2001 and 2006 indicates that the bow shock's structure is influenced by quasi-oscillatory density variations on scales as small as hundreds of au in the surrounding medium.

An unambiguous measurement of the electron density requires knowledge of the shock's inclination angle. Previous fitting by Chatterjee & Cordes (2002, 2004) for the inclination angle marginally constrained the bow shock to lie in the plane of the sky, and the closed-off, ringlike morphology of the bow

shock is broadly consistent with the Barkov et al. (2020) MHD simulations of the shock for large inclination angles. Assuming $i = 90°$, we find $n_{e,1994} = 0.44(5)$, $n_{e,2001} = 0.22(5)$, and $n_{e,2006} = 0.30(5)$ cm^{-3}. For an inclination angle $30°$ smaller or larger, the densities will be about 56% smaller. These densities are significantly larger than those inferred by Chatterjee & Cordes (2002, 2004), who used the NE2001 distance for the pulsar. The DM-derived distance based on NE2001 is 1.9 kpc, about twice as far as the recently observed parallax distance of 0.831 kpc (Deller et al. 2019), implying that the ISM along this LOS is denser than predicted by NE2001.

While the Wilkin (1996) thin-shell model is only adequate near the tip of the GN, the morphology of the downstream shock can still be used to assess the scales on which the assumption of uniform density in the Wilkin model breaks down. Figure 3 shows the outline of the head of the GN in each epoch with several realizations of the Wilkin model for different values of the projected standoff radius. In each epoch, the downstream shock is significantly broader than predicted by

Table 1
Hα-emitting Neutron Star Bow Shocks with Multiepoch Observations

			Neutron Star Properties			
PSR	J0437−4715	B0740−28	J1741−2054	J2030+4415	J2124−3358	B2224+65
DM (pc cm^{-3})	2.645	73.73	4.7	…	4.6	36.1
P (s)	5.8×10^{-3}	0.167	0.41	0.308	4.9×10^{-3}	0.68
$\dot{P}$ (10^{-20} s s^{-1})	5.73	1.68×10^{6}	1.7×10^{6}	6.5×10^{5}	2.06	9.66×10^{5}
π (mas)	6.396(54)	…	…	…	3.1(1)	1.20(19)
D (pc)	156	2070	300	750	323	831
μ_α (mas yr^{-1})	121.679(52)	−29	−63	15(11)	−14.14(4)	147.22(23)
μ_δ (mas yr^{-1})	−71.820(86)	4	−89	84(12)	−50.08(9)	126.53(19)
v_T (km s^{-1})	105	287	155	303	78	765
$\dot{E}_{33}$ (erg s^{-1})	5.5	140	9.5	22	6.8	1.2

			Bow Shock Properties			
Epoch 1	1993[a]	2001[b]	2009[c]	2011[d]	2001[e]	1994
Epoch 2	2012[d]	2013[d]	2015[f]	2015[g]	2013[d]	2001
Epoch 3	…	…	…	…	2015[h]	2006
$\theta_{a,1}$ (arcsec)	9.0	1.3	1.5[i]	1.1	2.6	0.077
$\theta_{a,2}$ (arcsec)	9.3	1.4	…	0.5[j]	5.0[k]	0.11
$\theta_{a,3}$ (arcsec)	…	…	…	…	2.73	0.094

Notes. Parallax (π), distance (D), and proper motion in R.A. (including cosδ) and decl. (μ_α, μ_δ) are from the following references: Deller et al. (2008) for J0437−4715, Reardon et al. (2016) for J2124−3358, and Deller et al. (2019) for B2224+65. The distances for B0740−28 and J1741−2054 are based on NE2001 (Cordes & Lazio 2002). Object J2030+4415 is a radio-quiet pulsar, and the quoted properties are based on γ-ray pulsations (Pletsch et al. 2012) and X-ray astrometry (de Vries & Romani 2020). All other neutron star properties are retrieved from the Australia Telescope National Facility Pulsar Catalogue (Manchester et al. 2005) unless otherwise noted. The bow shock apex distances θ_a are from the following references.
[a] Bell et al. (1993).
[b] Jones et al. (2002).
[c] Romani et al. (2010).
[d] Brownsberger & Romani (2014).
[e] Gaensler et al. (2002).
[f] Mignani et al. (2016).
[g] de Vries & Romani (2020).
[h] Romani et al. (2017).
[i] Romani et al. (2010) found an inclination angle $i = 80°$ for J1741−2054. No θ_a is listed for the second epoch because Mignani et al. (2016) found no evidence of a change in the standoff radius.
[j] This value of θ_a for J2030+4415 is only a nominal estimate from de Vries & Romani (2020), but this bow shock's complex, closed-bubble morphology suggests that more rigorous fitting for the inclination angle is needed.
[k] Brownsberger & Romani (2014) multiplied θ_a for J2124−3358 by a factor of 2 to account for possible projection effects, but more detailed modeling by Romani et al. (2017) found that θ_a is broadly consistent with the earlier Gaensler et al. (2002) result but with $i \approx 120°$.
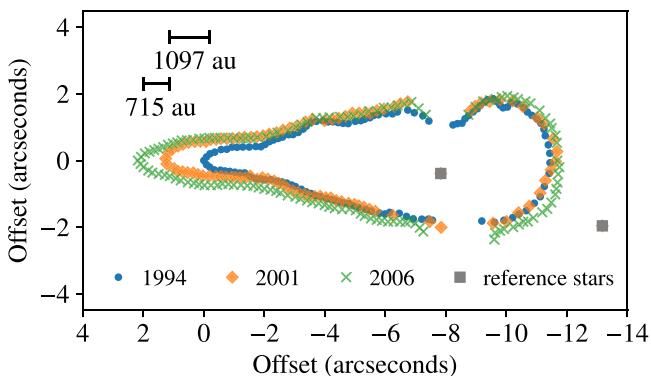

Figure 2. Outline of the limb-brightened head of the GN with the tip of the bow shock in 1994 set at the origin. The 1994, 2001, and 2006 epochs are shown as blue circles, orange diamonds, and green crosses, respectively. The gray squares show two of the three reference stars used to align the three epochs. The spatial offsets between the bow shock nose in 1994, 2001, and 2006 are also indicated.

the thin-shell model fit within 2″ of the nose. The downstream shock is also consistent with density variations on roughly

arcsecond scales, but these density variations do not have a consistent spatial periodicity. In addition, the bow shock structure is asymmetric, and this asymmetry does not necessarily translate uniformly from epoch to epoch. Variability in the observed asymmetry of the shock may be related to the shock's expansion into a medium that is nonuniform both parallel and transverse to the pulsar's proper motion, rather than related to, e.g., anisotropy in the pulsar wind (Vigelius et al. 2007). However, Figure 2 demonstrates that the downstream shock remains almost stationary between epochs, suggesting that the expansion rate downstream is significantly slower than at the nose. Apparent asymmetries in earlier observations of the shock may become smoothed out over time as thermal pressure modifies the morphology of the downstream shock, as discussed in Vigelius et al. (2007).

In Section 6, we calculate the turbulence spectrum of ionized interstellar gas around the GN using two methods: (1) epoch-to-epoch variations in the standoff radius fit only near the shock apex and (2) differences between standoff radii fit to different portions of the downstream shock within each epoch. In the first case, epoch-to-epoch density variations are calculated using the standoff radii fit to the shock apex (within 2″) and an
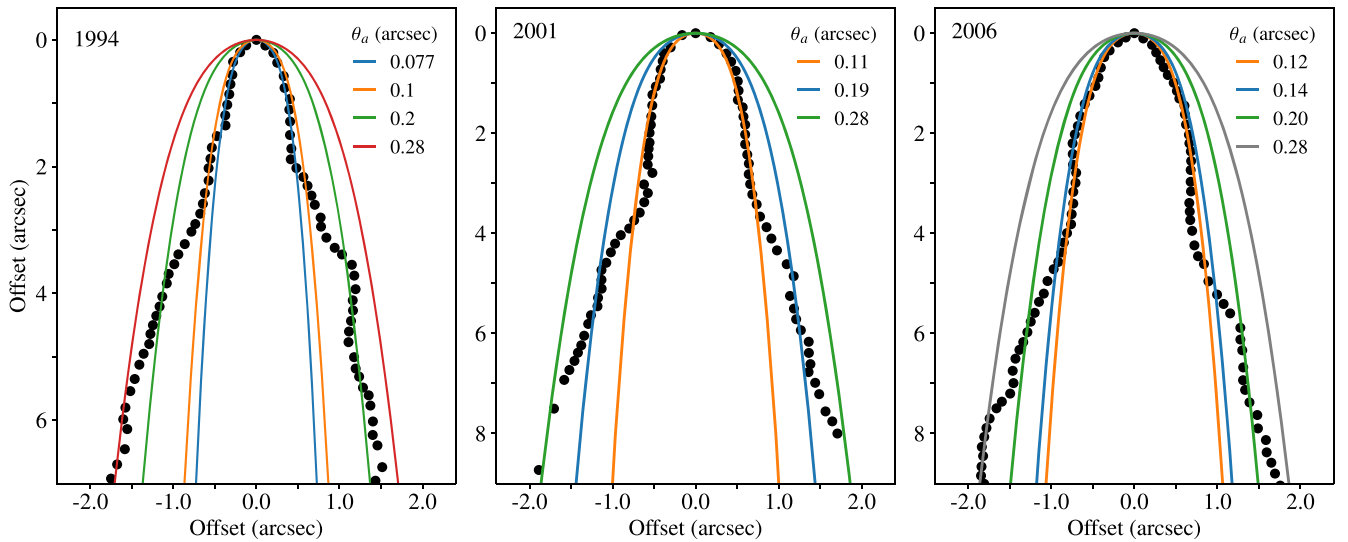
Figure 3. Outline of the limb-brightened head of the GN with the tip of the bow shock in each epoch set to the origin, which is aligned with the pulsar proper motion. The Wilkin (1996) model is shown for different values of the bow shock's projected angular apex distance.

inclination angle $i = 90°$ (see Equation (9)), and the resulting turbulence spectral amplitudes are calculated using Equation (5). The associated wavenumbers are calculated using the distance traversed by the pulsar between epochs. For three epochs (1994, 2001, and 2006), this epoch-to-epoch analysis yields three point estimates of the spectral amplitude and wavenumber. In the second method, we estimate density variations using standoff radii fit to different portions of the downstream shock within a given epoch. For the models shown in Figure 3, we calculate the differences in standoff radii between models that fit portions of the downstream shock and the model that fits within $2''$ of the apex. These differences yield rough estimates of density changes between gas around the downstream shock and gas near the shock apex and hence an estimate of the turbulence spectral amplitude. This second method only considers inhomogeneity of the shock structure within individual epochs, rather than epoch-to-epoch changes. This second method also ignores a number of processes that could modify the morphology of the downstream shock (as discussed in the previous paragraph) and is less rigorous than epoch-to-epoch density variations inferred from only the shock apex. However, accounting for the inhomogeneity of the downstream shock vastly expands the range of wavenumbers that may be probed to $10^{-15} \text{ m}^{-1} \lesssim q \lesssim 10^{-13} \text{ m}^{-1}$. The error associated with fitting standoff radii to the downstream shock is also orders of magnitude smaller than the spread of spectral amplitudes fit for the GN, which span over 6 orders of magnitude in the density fluctuation power spectrum. The turbulence spectral amplitudes obtained for the GN from both of the methods described are shown in Section 6.

4.2. Glitches

Between 1976 and 2007, B2224+65 had five reported glitches, the first and largest of which was reported by Backus et al. (1982). The glitch properties are shown in Table 2. The magnitude of a glitch is typically expressed as the fractional change in spin frequency $\Delta\nu/\nu$ and frequency derivative $\Delta\dot\nu/\dot\nu$ during a glitch. The fractional change in spin-down luminosity during a glitch, $\Delta\dot{E}/\dot{E}$, can be directly calculated from the change in ν and $\dot\nu$. For the simplest case, where no change in

frequency derivative is detected, $\Delta\dot\nu = 0$ and $\Delta\dot{E}/\dot{E} = \Delta\nu/\nu$. For typical cases, where $|\Delta\dot\nu| > 0$, $\Delta\dot{E}/\dot{E}$ must be explicitly calculated from the pre- and postglitch timing solutions, $\Delta\dot{E}/\dot{E} = (\nu_2\dot\nu_2 - \nu_1\dot\nu_1)/\nu_1\dot\nu_1$, where subscripts 1 and 2 refer to pre- and postglitch, respectively.

The fractional change $\Delta\dot{E}/\dot{E}$ and the corresponding change in standoff radius $\Delta R_0/R_0$ during each glitch are shown in Table 2. The estimates of $\Delta R_0/R_0$ assume a constant density during the glitch. Even for the largest glitch in 1976, the implied change in standoff radius is only 0.1%, smaller than the spatial resolution of the Hα images. The locations of the pulsar during each glitch are superimposed on the HST image from 2006 in Figure 4. There is no discernible correlation between the locations of the glitches and the bow shock morphology.

While we have only considered the change in spin-down luminosity in Table 2, it is unclear how much additional energy is processed through the pulsar wind during a glitch and whether this additional energy could significantly alter the standoff radius of a bow shock. Various magnetospheric effects have been observed during other pulsar glitches, including pulse shape changes in the Vela pulsar (Palfreyman et al. 2018), soft X-ray polarization changes in the Crab pulsar (Feng et al. 2020), and a pulse shape change in PSR B2021+51 (Liu et al. 2021). Such magnetospheric effects demonstrate that glitches may release additional energy that might impact the pulsar wind beyond the change in spin-down rate, but these effects are not a universal trait of glitches (Shaw et al. 2018; Jankowski et al. 2021) and have not been observed in any of the glitches from B2224+65.

In the case of B2224+65, the only empirical handles on energy loss during its glitches are ν and $\dot\nu$. In addition to converting $\Delta\dot{E}/\dot{E}$ to $\Delta R_0/R_0$, as shown in Table 2, we can estimate the instantaneous change in spin energy during a glitch as $\Delta E \approx I\Omega\Delta\Omega \approx 2(\Delta\Omega/\Omega)E$, which is about $10^{-6}E \approx 4 \times 10^{46}$ erg for the largest glitch in 1976. The glitch timescale is limited by the observation windows and constrained to the time period between 1976 September 13 and 1976 November 26 (Backus et al. 1982). Adopting 1.5 months as a conservative estimate of the glitch timescale, we have $\Delta\dot{E} \approx \Delta E/\Delta t \approx 10^{40}$ erg s^{-1}. If all of this energy were converted into the pulsar wind, then $\Delta R_0/R_0$ would be as large
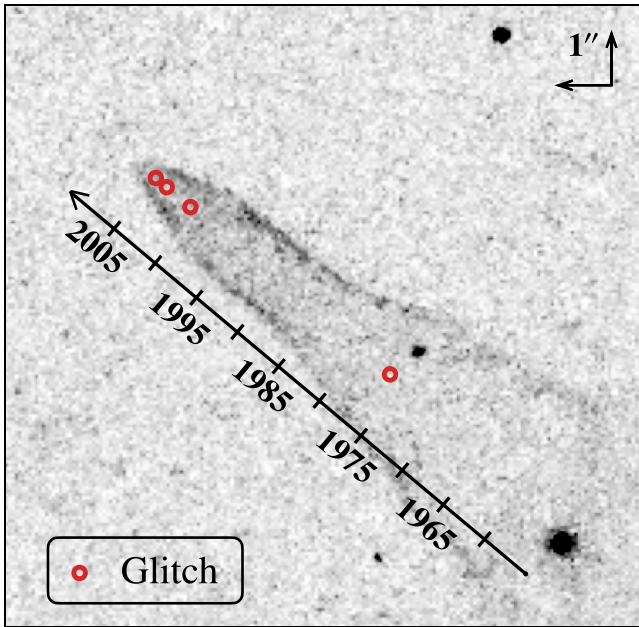
Figure 4. Locations of the pulsar during the four glitches reported between 1976 and 2005, overlaid as red open circles on the HST image of the Guitar from 2006. The solid black line indicates the direction of the pulsar's proper motion, with tick marks indicating the location of the pulsar every 5 yr along its historical trajectory.

Table 2
PSR B2224+65: Glitches

Year	$\Delta\nu/\nu$ (10^{-9})	$\Delta\dot\nu/\dot\nu$ (10^{-3})	$\Delta\dot E/\dot E$ (10^{-9})	$\Delta R_0/R_0$
1976[1,2]	$1.707(1) \times 10^3$	−3(5)	1707	0.0013
2000[3]	0.14(3)	−2.9(2)	⋯	⋯
2003[3]	0.08(4)	−1.4(2)	⋯	⋯
2005[3]	0.19(6)	⋯	0.19	1.4×10^{-5}
2007[4]	0.39(7)	−0.6(4)	0.39	1.9×10^{-5}

Note. Left to right: year and fractional changes in spin frequency $\Delta\nu/\nu$, spin frequency derivative $\Delta\dot\nu/\dot\nu$, spin-down luminosity $\Delta\dot E/\dot E$, and bow shock standoff radius $\Delta R_0/R_0$ for each glitch. The changes in standoff radius were calculated assuming a constant density during the glitches. Values of $\Delta\dot E/\dot E$ and $\Delta R_0/R_0$ are not shown for the 2000 and 2003 glitches because they do not have published pre- and postglitch timing solutions. For the other glitches, $\Delta\dot\nu/\dot\nu$ was ignored due to its large uncertainty. References: (1) Backus et al. (1982), (2) Shemar & Lyne (1996), (3) Janssen & Stappers (2006), (4) Yuan et al. (2010).

as 1000, and we would expect a substantial physical imprint of the glitch on the GN's structure. However, it is unclear if this spin energy is mediated through the pulsar wind or other processes like electromagnetic radiation, and for the three most recent glitches, the implied glitch energies are far too small to cause any detectable change in the standoff radius. Moreover, the energy release from glitches would most likely increase the standoff radius, whereas the narrowing of the bow shock apex during the three most recent glitches indicates that the standoff radius is decreasing. Glitches therefore appear to have a negligible impact on the observed morphology of the GN, suggesting that interstellar density fluctuations are likely the main driver of the standoff radius variations inferred from images of the GN.

However, we cannot rule out the general possibility that large glitches may impact the morphology of pulsar bow shocks, regardless of whether it appears to be a relevant effect for our analysis of the GN. For example, the quasiperiodically nulling pulsar B1931+24 exhibits a 50% increase in its spin-down rate during 5–10 day long active phases (Kramer et al. 2006). In this case, quasiperiodic variations in the standoff radius would occur between the active and inactive phases. If this pulsar has an Hα bow shock, then it would provide an ideal test bed for determining whether substantial changes in spin-down rate can be identified in large-scale bow shock images. We note, however, that even if B2224+65 experienced spin-down behaviors as extreme as those of B1931+24, the impact on the bow shock structure would likely be undetected because the timescale of the spin-down variations is much less than a year, the approximate timescale on which variations in the bow shock structure are resolved.

4.3. Comparison to Other Pulsar Bow Shocks

At the time of this work, five other neutron stars with Hα-emitting bow shocks had been observed over multiple epochs spanning years to decades: J0437−4715 (Bell et al. 1993, 1995; Brownsberger & Romani 2014), B0740−28 (Jones et al. 2002; Brownsberger & Romani 2014), J1741−2054 (Romani et al. 2010; Mignani et al. 2016), J2030+4415 (Brownsberger & Romani 2014; de Vries & Romani 2020), and J2124−3358 (Gaensler et al. 2002; Brownsberger & Romani 2014; Romani et al. 2017). Of these bow shocks, all but that of J0437−4715 show complex morphologies including closed bubbles, asymmetries, and undulating structures reminiscent of the Guitar (for a compilation of characteristic images, see Brownsberger & Romani 2014). The shock apex distances θ_a inferred by previous works are shown in Table 1. Previous studies generally quote an empirically measured θ_a and assume an inclination angle $i = 90°$, but some studies (Romani et al. 2010 for J1741−2054 and Romani et al. 2017 for J2124−3358) perform more complicated fits for the standoff radius and inclination angle simultaneously, and apex distances that are fit with different methods should not be considered as necessarily compatible, even for the same bow shock. Various published images of each bow shock are also generally obtained from different telescopes and instruments and hence vary in terms of resolution, seeing, and exposure time. Rather than reanalyze publicly available images of each bow shock in a self-consistent manner (which we relegate to future work), we adopt variations in the standoff radii quoted from various studies as upper limits, and in Section 6, we calculate upper limits on the density wavenumber spectrum for each bow shock accordingly.

5. Turbulence in the VLISM

5.1. Plasma Oscillations

The V1 measures the electron density of interstellar space by detecting plasma oscillations with the PWS (Gurnett et al. 2013). The PWS wideband receiver obtains voltage time series sampled at a rate of 28.8 kHz that are stored for later transmission to ground. These voltage time series are then converted to a frequency–time dynamic spectrum by Fourier methods, although automatic gain control on the wideband receiver prevents this spectrum from being calibrated to absolute electric field intensities. Nonetheless, the frequency
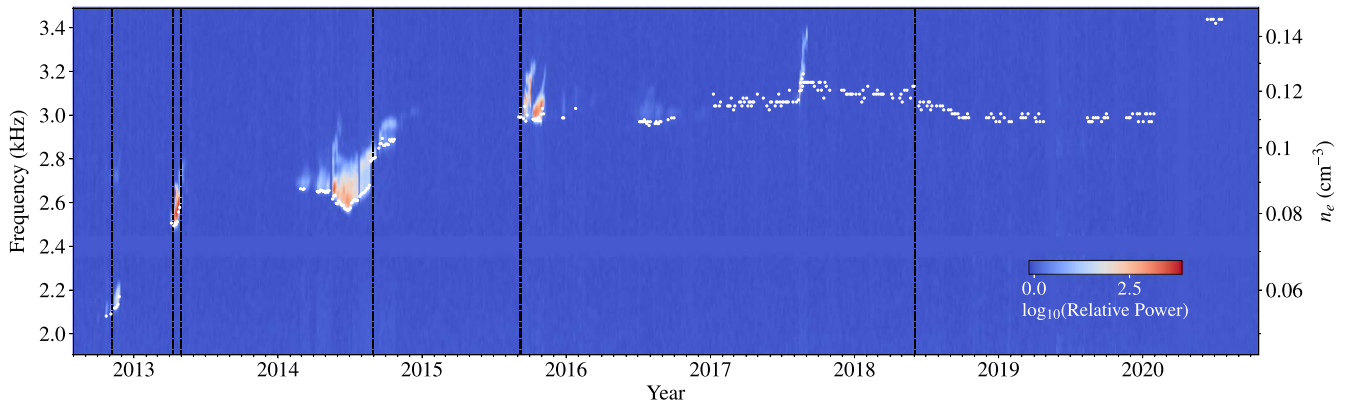
Figure 5. Dynamic spectrum showing all data from the V1 PWS wideband receiver since V1 crossed the heliopause on 2012 August 25. The time resolution of the spectrum is 3 days, and the frequency resolution is 0.011 kHz. Each column of pixels corresponds to a 1D spectrum that is the average of all 48 s epochs that fall within a given time bin and have been equilibrated to the same noise baseline. The power supply interference line at 2.4 kHz is masked, and data dropouts and periods of degraded telemetry are also masked. The spectrum is smoothed in frequency using a Gaussian kernel with $\sigma = 0.01$ kHz. Black dashed lines indicate epochs that were used to calculate density variations on 0.36 s timescales (see Figure 7), while the white points show average densities inferred from each epoch. The white points between 2017 and 2020 correspond to densities measured using techniques outlined in Ocker et al. (2021).

of plasma oscillations detected in the PWS spectrum can be used to infer the plasma density. All of the data from the V1 PWS wideband receiver from V1's crossing of the heliopause in 2012 through late 2020 are shown in Figure 5.

Plasma oscillations are found in the PWS spectrum in two main ways. The first occurs when shocks from solar coronal mass ejections trigger plasma oscillation events (POEs) seen by V1 as brief, days- to year-long bursts of power in the PWS spectrum, and these events often exhibit extended frequency structure and sharp monotonic increases in the plasma frequency that are associated with shocks passing over the spacecraft (Gurnett et al. 2015, 2021). The POEs have been detected by V1 approximately once per year since 2012, and their large intensities can allow the plasma frequency to be measured down to the smallest temporal resolution in the PWS spectrum, typically about 0.4 s. As V1 travels at a speed of about 17 km s^{-1}, the PWS spectrum can, at least in theory, resolve density fluctuations on scales as small as about 7 km.

The second class of plasma oscillations found by V1 are extremely weak, narrowband plasma oscillations that are detected in data from early 2017 through mid-2020 (Ocker et al. 2021). While the physical origin of these persistent plasma waves is not entirely clear, they are detectable in the absence of POEs and do not appear to be associated with solar-origin shocks. The low signal-to-noise ratio (S/N) of the persistent plasma waves means that they are only detectable after averaging over at least one epoch of V1 PWS data; hence, they can be used to resolve density fluctuations on length scales as small as about 0.03 au. The combined density time series from both POEs and persistent plasma waves constrains the density fluctuation spectrum over wavenumbers in the range 10^{-12} m$^{-1} \lesssim q \lesssim 10^{-3}$ m^{-1}.

5.2. Plasma Frequency Measurements

5.2.1. High Wavenumber Regime

In order to measure the plasma frequency over the smallest spatial scales, we extracted six single epochs of PWS data during POEs, indicated by the black lines in Figure 5. During these epochs, the plasma line had a narrow bandwidth (≈ 0.05 kHz) and high S/N (>10), allowing for precise characterization of variations in the plasma frequency over

the shortest timescales within a given epoch. An example of one of these epochs is shown in Figure 6(a). The plasma frequency was measured using a 1D matched filtering approach, where each column of the 2D spectrum was convolved with a Gaussian pulse in frequency space. The plasma frequency corresponds to the lower-frequency cutoff of the plasma oscillations, which was taken to be the lower edge of the FWHM (e.g., Gurnett & Kurth 2019; Lee & Lee 2019, 2020). Figure 6(a) also shows 1D slices through the spectrum at different times during the observation, demonstrating amplitude variations in the intensity of the plasma line. These amplitude variations do not impact the plasma frequency extraction due to the narrow bandwidth and high S/N of the plasma line. The plasma frequencies and corresponding densities for all six epochs are shown in Figure 7.

While the POEs are generally detected within individual PWS epochs to high S/N, they typically exhibit a range of complex variability that makes it difficult to differentiate between plasma frequency variations related to changes in the underlying density and variations associated with wave interactions or the instrumental quantization of the signal. Almost every POE displays a combination of plasma oscillation sidebands, which are typically attributed to Langmuir parametric decay and the excitation of higher wave modes, and trapped radio emissions that augment the plasma line (e.g., Gurnett et al. 2013). In many cases, the plasma oscillation sidebands vary in intensity within a single epoch, making it difficult to accurately track the lowest-frequency sideband that would be attributed to the plasma frequency. Epochs where the plasma line is dominated by broadband radio emissions also display a large degree of variability over the shortest timescales, and it is unclear whether apparent frequency variations during these epochs are an accurate measure of the underlying density. A typical example of an epoch containing broadband radio emission is shown in Figure 6(b). Instrumental quantization further complicates interpretation of the apparent variability in these epochs, as the finite frequency resolution of the spectrum can effectively smear out or even enhance apparent frequency variations when the plasma line contains sidebands or broadband radio emission. By contrast, the six epochs chosen to constrain density variations on the smallest
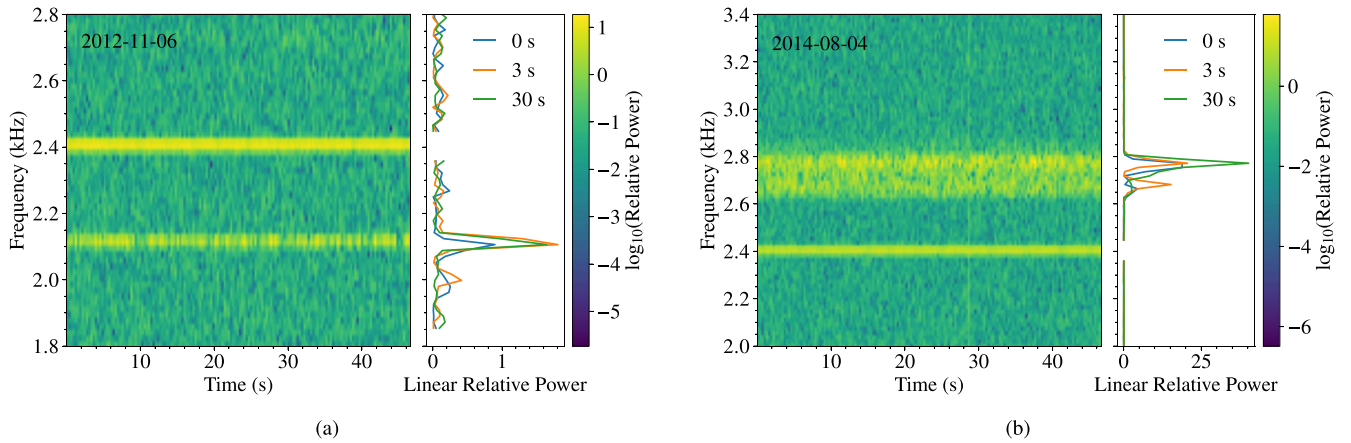
Figure 6. (a) Single epoch of V1 PWS data from 2012 November 6. The 2D dynamic spectrum has a temporal resolution of 0.36 s and a frequency resolution of 18 Hz, and it displays the plasma oscillation line at 2.1 kHz and the power supply interference line at 2.4 kHz. The 1D slices through the spectrum at 0, 3, and 30 s are also shown. (b) Single epoch of V1 PWS data from 2014 August 4. The 2D dynamic spectrum displays plasma oscillations with frequency structure extending from 2.6 to 2.8 kHz that is associated with radio emission and frequency sidebands. The 1D slices through the spectrum at 0, 3, and 30 s are also shown.

spatial scales are characterized by narrow plasma lines that do not contain any evidence of frequency sidebands or broadband emission. The narrow bandwidth of the plasma line during these epochs mitigates the signal quantization, but we nonetheless interpret the plasma frequency variations in these epochs as upper limits on the underlying turbulent density variations.

5.2.2. Low Wavenumber Regime

Despite the complex variability displayed in most epochs containing POEs, the shape of the plasma line is generally stable when averaged over a full 48 s epoch. Therefore, to measure density variations in the low wavenumber regime and over the largest spatial scales, we extract the plasma frequency by averaging every epoch in time to obtain a 1D spectrum that is then analyzed through the same matched filtering technique applied to the individual epochs described in Section 5.2.1. The resulting densities are overlaid on the full PWS spectrum in Figure 5. We also extract the persistent, narrowband plasma waves apparent in the PWS spectrum beginning in early 2017 using the same techniques outlined in Ocker et al. (2021). Our analysis includes newer data extending through 2020 October, when the frequency of the persistent plasma line increases by a factor of about 1.1 due to the passage of a magnetic pressure front over the spacecraft (Burlaga et al. 2021). The densities extracted from the persistent plasma waves are also shown in Figure 5. We ignore several epochs bordering shock discontinuities in the 2014 and 2017 POEs because these discontinuities do not reflect a turbulent process.

6. Results: The Composite Wavenumber Spectrum

The electron density measurements obtained from the GN and V1 PWS are used to calculate the wavenumber spectrum of density fluctuations using the analytic formalism described in Section 2 and fixing the spectral index to $\beta = 11/3$. The resulting spectrum is shown in Figure 8. The spectral amplitudes obtained by fitting the Wilkin model to the tip of the GN and various sections of the downstream shock are shown separately in Figure 8 and are consistent with a mean spectral amplitude $C_n^2 = 10^{-0.8 \pm 0.2}$ m$^{-20/3}$. Figure 8 also

shows upper limits on point estimates of $\widehat{C}_n^2$ for four other pulsar bow shocks described in Section 4.3.

Owing to the temporal resolution and sampling of the V1 data on both short and long timescales, the spectrum of V1 densities falls into two wavenumber regimes: $q \gtrsim 10^{-5}$ m^{-1} and 10^{-12} m$^{-1} \lesssim q \lesssim 10^{-8}$ m^{-1}. In both cases, the density structure function was binned in wavenumber space and then averaged to obtain a single constraint $\widehat{C}_n^2$ per wavenumber bin. In the low wavenumber regime, density measurements are obtained from both POEs and persistent narrowband plasma waves. The wavenumber spectrum obtained solely from the persistent plasma waves yields $C_n^2 \approx 10^{-1.6}$ m$^{-20/3}$ (Ocker et al. 2021), and when we include POE densities, the best-fit spectral amplitude obtained through nonlinear least-squares fitting is $C_n^2 = 10^{-1.57 \pm 0.02}$ m$^{-20/3}$; this fit ignores $q < 1.5 \times 10^{-12}$ m^{-1} owing to a spectral excess discussed later. The spectral amplitude errors for both the Guitar and V1 are only based on the fit for C_n^2 from the data and do not account for statistical variations associated with sampling a single realization of a Kolmogorov process. We therefore interpret the spectral amplitude errors for both the GN and V1 as lower limits on the true uncertainties.

Our constraint on C_n^2 for the VLISM probed by V1 is consistent with the Lee & Lee (2020) study that examined V1 data extending through 2019 June and found $C_n^2 = 10^{-1.47 \pm 0.04}$ m$^{-20/3}$. Similar to Lee & Lee (2019, 2020), we also find a power excess with a shallower spectral slope in the high wavenumber regime of the V1 spectrum. Lee & Lee (2019, 2020) suggested that this spectral excess at high wavenumbers may be associated with local kinetic wave activity that is triggered by the shocks responsible for POEs. It is possible that kinetic Alfvén waves are responsible for density fluctuations in the high wavenumber regime, and hence the observed spectral excess could be indicative of the underlying physical processes that are transmitting turbulence at these scales. However, constraints on the high wavenumber regime with V1 are ultimately limited by the finite resolution of the data in both time and frequency, and it remains possible that quantization of the PWS data on the shortest timescales may bias the observed density variations at the highest wavenumbers. We therefore interpret the amplitude
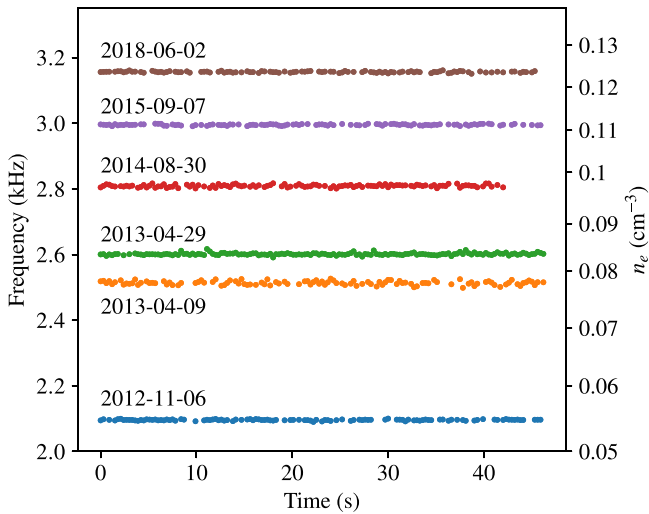
Figure 7. Plasma frequencies (left axis) and densities (right axis) measured for six epochs of V1 PWS data on short (0.36 s) timescales. Each epoch is about 48 s long, and gaps appear where the S/N was too low to accurately detect the plasma line. These epochs correspond to the black dashed lines in Figure 5 and were chosen based on the narrow bandwidth ($\approx$0.02–0.04 kHz) and high S/N of the plasma oscillations.

Figure 8. Bottom: 3D wavenumber spectrum of density fluctuations inferred from both in situ and integrated density measurements. The spectrum inferred from observations of the GN is shown in black for densities that were obtained using only the shock apex, where Wilkin (1996) provided a more precise constraint on the standoff radius, and light blue for densities that were obtained by extrapolating Wilkin (1996) to various parts of the downstream shock. Squares with error bars for the Guitar indicate the range of $\widehat{C}_n^2$ for $i = 90° \pm 30°$. Triangles indicate spectral constraints based on four other pulsar bow shocks: J0437−4715, B0740−28, J2030+4415, and J2124−3358. These spectral amplitudes are presented as upper limits (see Section 4.3). The spectra of densities obtained with V1 are colored according to the type of plasma wave phenomena used: green for POEs, blue for persistent plasma waves (PPWs) spanning 2017–2020, and orange for a combination of POEs and the PPW data. The spectral amplitudes shown for V1 are binned in wavenumber space and then averaged, but the full distribution of amplitudes is shown by the smaller translucent green and orange points. Constraints from pulsar DM variations over time (DM(t)) are shown as gray crosses. The solid lines indicate the best-fit spectral amplitudes for the GN (light blue) and V1 data (black). The dashed line indicates a constant amplitude $C_n^2 = 10^{-3.5}$ m$^{-20/3}$. Top: all estimated spectral amplitudes divided by the best-fit value for the VLISM probed by V1, $C_n^2 \approx 10^{-1.57}$ m$^{-20/3}$.

of the V1 density spectrum as an upper limit in this high wavenumber regime.

A power excess is also found at the lowest wavenumbers ($q < 1.5 \times 10^{-12}$ m^{-1}) of the V1 spectrum and is likely related to density variations over the largest spatial scales in the V1 data. At these scales, the observed density variations are influenced by a combination of turbulent and deterministic processes, like the discrete shocks that trigger POEs and cause density jumps in the PWS spectrum. It can be difficult to disentangle solar-origin shocks from the underlying structure of the VLISM, which is largely determined by interactions between the interstellar plasma and magnetic fields with those of the solar wind. For example, between 2013 and 2015, multiple density jumps are observed in the PWS spectrum, two of which are directly associated with shock waves observed in the V1 magnetic field data (Burlaga et al. 2013; Gurnett et al. 2015). However, the rise in density between 2013 and 2015 also appears to be a persistent, structural feature of the VLISM, as the density remains roughly constant from 2015 through early 2020, when another magnetic pressure wave and density jump are observed (Burlaga et al. 2021). While we ignore two well-defined shock discontinuities when calculating the V1 wavenumber spectrum, the spectral excess at low wavenumbers is likely still biased by discrete structural variations in the plasma between the heliopause and solar system bow shock/wave.

The spectra of density fluctuations observed near the GN, near the other four pulsar bow shocks examined, and in the VLISM are all consistent with a turbulence spectrum that is enhanced when compared to other pulsars' LOSs through the local ISM. In Figure 8, we show constraints on the wavenumber spectrum from DM variations observed in the Nanohertz Observatory for Gravitational Waves (NANOGrav) 12.5 yr data set (Alam et al. 2021). The DM time series of 18 pulsars were chosen based on consistency of the DM structure functions with a Kolmogorov process, and the spectral amplitudes were then calculated from the DM structure functions according to Equation (6). Small temporal lags in the DM structure functions were ignored due to biasing from
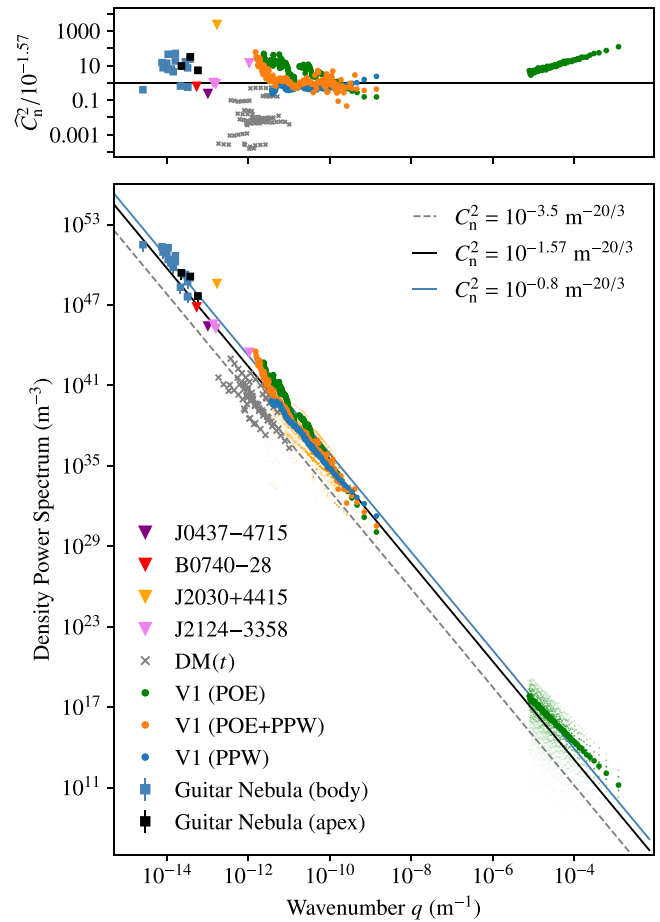
white noise, and large temporal lags were similarly ignored due to biasing from the finite length of the data set. The resulting structure functions constrain C_n^2 over wavenumbers 10^{-13} m$^{-1} \lesssim q \lesssim 10^{-11}$ m^{-1}. The DM variations are broadly consistent with $C_n^2 \approx 10^{-3.5}$ m$^{-20/3}$, the typical value that has been found in previous studies of the turbulence spectrum in the warm ionized medium (WIM; e.g., Armstrong et al. 1995; Chepurnov & Lazarian 2010). The DM(t) wavenumber spectrum also exhibits an orders-of-magnitude spread in C_n^2 that reflects large variations between different LOSs through the local ISM.

7. Discussion

We present electron density fluctuation measurements obtained from Hα images of the GN and from V1 PWS and constrain the density wavenumber spectrum over spatial scales of kilometers to thousands of au. The characteristic electron densities in these regions are $n_e \sim 0.3$ cm^{-3} for the GN and $n_e \sim 0.1$ cm^{-3} for the VLISM. Comparison to previous observations of four other pulsar bow shocks shows that all of the bow shocks examined in this study exhibit a spectral amplitude C_n^2 that is orders of magnitude larger than values that are considered typical in the WIM. For the GN, we find $C_n^2 = 10^{-0.8 \pm 0.2}$ m$^{-20/3}$, and for the VLISM probed by V1, we find $C_n^2 = 10^{-1.57 \pm 0.02}$ m$^{-20/3}$.

It has already been suggested that the large value of C_n^2 in the VLISM is the result of a turbulence spectrum that is enhanced by the superposition of interstellar and solar wind turbulence (Zank et al. 2019). If that is the case, it is unclear how far Voyager would need to travel to sample "pristine" or "quiescent" interstellar turbulence, although it is likely that Voyager would need to cross the heliospheric bow shock/wave. Nonetheless, beyond the heliospheric bow wave lies a collection of interstellar clouds (one of which encases the solar system; Linsky et al. 2019), and cloud–cloud interactions may further modify turbulent density variations in this region (Redfield & Linsky 2004). It is unclear whether interactions between a bow shock and the ISM lead to similarly large values of C_n^2 for the GN and the other bow shocks considered in this work. We find no empirical evidence that discrete events from B2224+65, such as glitches, have any observable impact on the GN's structure and inferred density fluctuations. Moreover, the large range of C_n^2 that we estimate from DM variations along a number of pulsar LOSs suggests that apparent enhancements to C_n^2 for the VLISM and the pulsar bow shocks considered may simply reflect larger-scale variability between different regions of the ionized ISM.

It is also possible that Hα detections of pulsar bow shocks are systematically biased toward regions of higher density, leading to a higher C_n^2 than expected from pulsar DMs and scattering measurements. Pulsar bow shocks will only produce visible Hα emission when the neutral fraction in the surrounding gas is large enough, although exactly how large it needs to be depends on other factors, like the pulsar velocity and distance (Chatterjee & Cordes 2002; Brownsberger & Romani 2014). Generally speaking, the number densities of cold and warm neutral gas in the ISM are much larger ($n_H \sim 30$ and ~ 0.6 cm^{-3}, respectively) than densities characteristic of the WIM (~ 0.01 cm^{-3}; Draine 2011). The pulsars producing these bow shocks may also preionize the atomic gas, leading to a higher electron density (Lam et al. 2016).

In this case, linear DM variations may also be detected from the pulsars due to their motions away from or toward the observer, combined with discrete changes in DM caused by preionization of gas ahead of the shock and the pulsars moving through gas of varying density. If this is the case, shock-induced DM variations will largely be detected from pulsars residing in atomic gas, which comprises about 60% of the ISM (Draine 2011). Recent analysis of the NANOGrav 9 yr data set by Jones et al. (2017) found linear DM trends in 14 of the 37 pulsars analyzed (38%), but combinations of linear trends and other fluctuations were also found in an additional 14 of the 37 pulsars. It is possible that some of these linear DM variations are related to pulsar bow shocks residing in atomic gas. In our analysis, we focus on stochastic DM variations that are easily attributable to turbulent density fluctuations. The DM variations are only sensitive to free electrons and are integrated over tens of parsecs to kiloparsec-scale distances, and in the absence of large-scale, discrete structures along the LOS, stochastic DM variations will generally trace the more diffuse WIM. We could therefore interpret the broad range of C_n^2 estimated from the stochastic DM variations analyzed in this study as a reflection of a WIM that varies in structure and is permeated by H II regions and bubbles, whereas estimates of C_n^2 based on pulsar bow shocks may generally trace denser, more neutral media. If this is the case, then continued comparison of density fluctuations from direct observations of bow shocks and remote observations of pulsar DM and scattering may allow us to distinguish the properties of turbulence for a range of gas conditions in the ISM.

Previous studies on the density and magnetic field power spectra of interstellar turbulence in the ionized components of the ISM have generally focused on consistency with a Kolmogorov spectral index over many decades in wavenumber. In this study, we aim to call attention to departures from a uniform turbulence spectrum. Not only do we find large variability in the spectral amplitude between different pulsars' LOSs through the ISM, we also find significant enhancements in the spectral amplitude near the solar system bow shock/wave and for the pulsar bow shocks considered. It is unclear whether these enhanced spectral amplitudes are characteristic of stellar bow shocks in general and hence represent some local feature of turbulence in these environments. Given that the ISM is permeated by stars emitting winds and flares, high-velocity stars driving shocks, and supernovae, the mechanisms by which turbulence is mediated through these various phenomena is of high interest. Previous studies have already demonstrated that additional properties of the turbulence spectrum, such as the outer and inner scales, sonic regime, and spectral amplitude and slope, may vary between different regions of the local ISM and across the Galaxy (e.g., Cordes et al. 1985; Krishnakumar et al. 2015). In the VLISM, the outer scale constrained by magnetic field and density fluctuations is about 0.01 pc (Burlaga et al. 2018; Lee & Lee 2020), whereas in the Galactic thick disk, the outer scale may be as large as 100 pc and will generally depend on the mechanisms that drive turbulence in a particular region, such as stellar winds and supernovae. Similarly, the inner scale may vary depending on the local magnetic field strength and resulting proton gyroradius. In future work, we will assess variations in the density wavenumber spectrum in the context of pulsar scattering measurements and their spatial distribution and evaluate these variations with respect to previous studies examining systematic differences between turbulence in the inner and outer Galaxy.

ORCID iDs

Stella Koch Ocker ◉ https://orcid.org/0000-0002-4941-5333
James M. Cordes ◉ https://orcid.org/0000-0002-4049-1882
Shami Chatterjee ◉ https://orcid.org/0000-0002-2878-1502
Timothy Dolch ◉ https://orcid.org/0000-0001-8885-6388

References

Alam, M. F., Arzoumanian, Z., Baker, P. T., et al. 2021, ApJS, 252, 4
Aldcroft, T. L., Romani, R. W., & Cordes, J. M. 1992, ApJ, 400, 638
Armstrong, J. W., Rickett, B. J., & Spangler, S. R. 1995, ApJ, 443, 209
Backus, P. R., Taylor, J. H., & Damashek, M. 1982, ApJL, 255, L63
Barkov, M. V., Lyutikov, M., & Khangulyan, D. 2020, MNRAS, 497, 2605
Bell, J. F., Bailes, M., & Bessell, M. S. 1993, Natur, 364, 603
Bell, J. F., Bailes, M., Manchester, R. N., Weisberg, J. M., & Lyne, A. G. 1995, ApJL, 440, L81
Brownsberger, S., & Romani, R. W. 2014, ApJ, 784, 154
Bucciantini, N. 2002, A&A, 393, 629
Burlaga, L. F., Florinski, V., & Ness, N. F. 2018, ApJ, 854, 20
Burlaga, L. F., Kurth, W. S., Gurnett, D. A., et al. 2021, ApJ, 911, 61
Burlaga, L. F., Ness, N. F., Gurnett, D. A., & Kurth, W. S. 2013, ApJL, 778, L3
Chatterjee, S., & Cordes, J. M. 2002, ApJ, 575, 407
Chatterjee, S., & Cordes, J. M. 2004, ApJL, 600, L51
Chepurnov, A., & Lazarian, A. 2010, ApJ, 710, 853
Cordes, J. M., & Lazio, T. J. W. 2002, arXiv:astro-ph/0207156
Cordes, J. M., Romani, R. W., & Lundgren, S. C. 1993, Natur, 362, 133
Cordes, J. M., Weisberg, J. M., & Boriakoff, V. 1985, ApJ, 288, 221
de Vries, M., & Romani, R. W. 2020, ApJL, 896, L7
Decin, L., Cox, N. L. J., Royer, P., et al. 2012, A&A, 548, A113
Deller, A. T., Goss, W. M., Brisken, W. F., et al. 2019, ApJ, 875, 100
Deller, A. T., Verbiest, J. P. W., Tingay, S. J., & Bailes, M. 2008, ApJL, 685, L67
Dolch, T., Chatterjee, S., Clemens, D. P., et al. 2016, JASS, 33, 167
Draine, B. T. 2011, Physics of the Interstellar and Intergalactic Medium (Princeton, NJ: Princeton Univ. Press)
Feng, H., Li, H., Long, X., et al. 2020, NatAs, 4, 511
Gaensler, B. M., Jones, D. H., & Stappers, B. W. 2002, ApJL, 580, L137
Gautam, A., Chatterjee, S., Cordes, J. M., Deller, A. T., & Lazio, J. 2013, AAS Meeting Abstracts, 221, 154.04

Gurnett, D. A., & Kurth, W. S. 2019, NatAs, 3, 1024
Gurnett, D. A., Kurth, W. S., Burlaga, L. F., & Ness, N. F. 2013, Sci, 341, 1489
Gurnett, D. A., Kurth, W. S., Stone, E. C., et al. 2015, ApJ, 809, 121
Gurnett, D. A., Kurth, W. S., Stone, E. C., et al. 2021, AJ, 161, 11
Jankowski, F., Keane, E. F., & Stappers, B. W. 2021, MNRAS, 504, 406
Janssen, G. H., & Stappers, B. W. 2006, AAP, 457, 611
Jones, D. H., Stappers, B. W., & Gaensler, B. M. 2002, A&A, 389, L1
Jones, M. L., McLaughlin, M. A., Lam, M. T., et al. 2017, ApJ, 841, 125
Kargaltsev, O., Pavlov, G. G., Klingler, N., & Rangelov, B. 2017, JPlPh, 83, 635830501
Kramer, M., Lyne, A. G., O'Brien, J. T., Jordan, C. A., & Lorimer, D. R. 2006, Sci, 312, 549
Krishnakumar, M. A., Mitra, D., Naidu, A., Joshi, B. C., & Manoharan, P. K. 2015, ApJ, 804, 23
Lam, M. T., Cordes, J. M., Chatterjee, S., et al. 2016, ApJ, 821, 66
Lee, K. H., & Lee, L. C. 2019, NatAs, 3, 154
Lee, K. H., & Lee, L. C. 2020, ApJ, 904, 66
Linsky, J. L., Redfield, S., & Tilipman, D. 2019, ApJ, 886, 41
Liu, J., Wang, H.-G., Yan, Z., et al. 2021, ApJ, 912, 58
Manchester, R. N., Hobbs, G. B., Teoh, A., & Hobbs, M. 2005, AJ, 129, 1993
McComas, D. J., Alexashov, D., Bzowski, M., et al. 2012, Sci, 336, 1291
McComas, D. J., Bzowski, M., Frisch, P., et al. 2015, ApJ, 801, 28
Mignani, R. P., Testa, V., Marelli, M., et al. 2016, ApJ, 825, 151
Ocker, S. K., Cordes, J. M., Chatterjee, S., et al. 2021, NatAs, 5, 761
Opher, M. 2016, SSRv, 200, 475
Palfreyman, J., Dickey, J. M., Hotan, A., Ellingsen, S., & van Straten, W. 2018, Natur, 556, 219
Peri, C. S., Benaglia, P., Brookes, D. P., Stevens, I. R., & Isequilla, N. L. 2012, A&A, 538, A108
Peri, C. S., Benaglia, P., & Isequilla, N. L. 2015, A&A, 578, A45
Pletsch, H. J., Guillemot, L., Allen, B., et al. 2012, ApJ, 744, 105
Rangelov, B., Pavlov, G. G., Kargaltsev, O., et al. 2016, ApJ, 831, 129
Rangelov, B., Pavlov, G. G., Kargaltsev, O., et al. 2017, ApJ, 835, 264
Reardon, D. J., Hobbs, G., Coles, W., et al. 2016, MNRAS, 455, 1751
Redfield, S., & Linsky, J. L. 2004, ApJ, 613, 1004
Romani, R. W., Shaw, M. S., Camilo, F., Cotter, G., & Sivakoff, G. R. 2010, ApJ, 724, 908
Romani, R. W., Slane, P., & Green, A. W. 2017, ApJ, 851, 61
Shaw, B., Lyne, A. G., Stappers, B. W., et al. 2018, MNRAS, 478, 3832
Shemar, S. L., & Lyne, A. G. 1996, MNRAS, 282, 677
Shklovskii, I. S. 1970, SvA, 13, 562
Swaczyna, P., Bzowski, M., Kubiak, M. A., et al. 2018, ApJ, 854, 119
Toropina, O. D., Romanova, M. M., & Lovelace, R. V. E. 2019, MNRAS, 484, 1475
Vigelius, M., Melatos, A., Chatterjee, S., Gaensler, B. M., & Ghavamian, P. 2007, MNRAS, 374, 793
Wilkin, F. P. 1996, ApJL, 459, L31
Yoon, D., & Heinz, S. 2017, MNRAS, 464, 3297
Yuan, J. P., Wang, N., Manchester, R. N., & Liu, Z. Y. 2010, MNRAS, 404, 289
Zank, G. P., Heerikhuisen, J., Wood, B. E., et al. 2013, ApJ, 763, 20
Zank, G. P., Nakanotani, M., & Webb, G. M. 2019, ApJ, 887, 116
Zieger, B., Opher, M., Schwadron, N. A., McComas, D. J., & Tóth, G. 2013, GRL, 40, 2923